



Cu₂O/BiVO₄ heterostructure controllably triggers radical and non-radical persulfate activation via light “on-off” for efficient organic contaminants degradation

Chengbo Bai^{a,b}, Wenjin Guo^{a,b}, Qiong Liu^b, Guangfang Li^c, Sheng Guo^a, Rong Chen^{a,d,*}

^a State Key Laboratory of New Textile Materials & Advanced Processing Technologies, Wuhan Textile University, Wuhan 430200, PR China

^b School of Chemistry and Environmental Engineering, Wuhan Institute of Technology, Wuhan 430205, PR China

^c Key Laboratory of Material Chemistry for Energy Conversion and Storage (Ministry of Education), Hubei Key Laboratory of Material Chemistry and Service Failure, Huazhong University of Science and Technology, Wuhan 430074, PR China

^d Henan Institute of Advanced Technology, Zhengzhou University, Zhengzhou 450002, PR China

ARTICLE INFO

Keywords:

Cu₂O/BiVO₄

Persulfate

Radical and non-radical pathway

Light switch

ABSTRACT

The regulation of peroxydisulfate (PDS) activation pathway is crucial for its practical application in complicated water matrix. In this work, we have developed a Cu₂O/BiVO₄ (Cu-BVO) heterostructure to achieve controlled triggering of both radical and non-radical PDS activation by dexterously utilizing light “on-off” for highly efficient degradation of organic contaminants. In dark condition, Cu-BVO serves as an electron donor to facilitate the cleavage of O-O bond in PDS via a radical pathway to generate •OH and •O₂. Upon light irradiation, Cu-BVO unexpectedly acts as an electron acceptor in the reversed electron flow to generate a metastable surface complex (Cu-BVO-PDS*) via non-radical pathway. Analysis of the kinetic behavior of the excited electrons and holes suggests that the directional migration of photo-excited charge carriers in Cu-BVO results in the electron-deficient region on the Cu₂O surface, which provides an ideal platform for the generation of Cu-BVO-PDS*.

1. Introduction

Efficient persulfate-based advanced oxidation processes (PDS-AOPs) have been widely recognized as one of the most powerful techniques in wastewater treatments. Persulfate can be activated into radicals (•OH, •SO₄ and •O₂) and non-radical species through energy-transfer or reductive electron-transfer processes [1]. The strong oxidizing power of radicals (E_0 , •OH=1.9–2.7 V, E_0 , •SO₄=2.5–3.1 V) donates the radical-based AOP system efficient decomposing ability toward a broad spectrum of recalcitrant pollutants [2,3]. However, the coexisting inorganic anions and natural organic matters (NOM) in actual water can react with these highly reactive radicals and inhibited the oxidation efficiency in eliminating organic pollutants while potentially producing more toxic secondary contaminants [4–6]. Fortunately, persulfate could be activated into non-radical reactive species by manipulating the physicochemical properties of catalysts, which exhibits huge potential in complicated water environment [7]. Although non-radical processes possess lower oxidation and mineralization capacities compared to

radical activation methods, they hold immense practical value due to their resistance against scavengers and background substances present in water matrices [8].

Therefore, it is of great significance to regulate the activation pathway of PDS in order to effectively eliminate the organic pollutants in complex water environment. Despite numerous research efforts aimed at achieving controllable transformation of the PDS activation pathway, such as the proposed photo-switch for PDS activation over layered CuFe oxide, there is currently no powerful and in-situ evidence to confirm the switchable peroxydisulfate non-radical/radical activation [9]. The closest example is the transformation from radical PMS-activated process to the ¹O₂ based non-radical process through the incorporation of MgO into CuO/Fe₃O₄ catalyst [7]. To date, few catalytic systems has successfully achieved free switching of radical and non-radical PDS activation for organic pollutant degradation. It remains challenging to reasonably design materials to effectively mediate the interfacial bonding mode and the electron transfer process between the materials and PDS, leading to drive both radical and non-radical

* Corresponding author at: State Key Laboratory of New Textile Materials & Advanced Processing Technologies, Wuhan Textile University, Wuhan 430200, PR China.

E-mail address: rchenhku@hotmail.com (R. Chen).

<https://doi.org/10.1016/j.apcatb.2023.123606>

Received 24 September 2023; Received in revised form 1 December 2023; Accepted 9 December 2023

Available online 17 December 2023

0926-3373/© 2023 Elsevier B.V. All rights reserved.

pathway and realize their controllable conversion in the actual water environment. Alternately, although three mainstream non-radical pathways including electron-transfer processes (ETP), singlet oxygenation, and high-valent metal induced oxidation have been extensively reported [10–12], the underlying mechanisms are still ambiguous and debatable due to a lack of reliable characterization techniques capable of capturing the transition state reactive oxygen species (ROS) and distinguishing the different reaction pathways.

The binding mode and ability of materials towards PDS, as well as the activation pathways of PDS, can be influenced by factors such as surface charge distribution and spin state of metals. These factors impact reaction kinetics (electron transfer ability) and thermodynamics (reactant adsorption, activation, and evolution barriers and pathways) [13–16]. Unsaturated sites with high spin states have a stronger ability to give electrons, and unpaired electrons will break the O–O bond of PDS through the single-electron pathway to produce radicals. The sites with low spin states are more likely to provide empty orbitals for electron shuttle in the electron transfer process (ETP) and promote the formation of surface-active complexes. The electron transfer process between metal and PDS is crucial in this process [13]. Therefore, it is reasonable to believe that it would be an effective strategy to regulate the interfacial binding mode and electron transfer process between materials and PDS by tuning the composition and surface chemical state, so as to realize the free switching of radical and non-radical PDS activation pathway. If the charge distribution around the surface of the metal center can be effectively regulated to alter the interface bonding mode between the material and PDS, it is expected to change the activation mode of PDS [17,18]. It is well known that semiconductor photocatalysis is achieved by carrier transfer in essence, in which photogenerated electron-hole migration of heterojunction materials could effectively mediate the surface chemical state of the catalyst [19–23]. Considering that the photoelectron-hole migration of heterojunction semiconductor photocatalytic materials can effectively mediate the surface chemical state of the catalyst [24,25], therefore, we believe that we can use the light "on-off" to vary the carrier transfer and thus freely regulate the radical and non-radical activation pathways of PDS. Recently, Cu-based heterojunctions have garnered significant attention due to their effective activity in both PDS and PMS activation, as well as their diverse activation pathways in the PDS/PMS activation processes. Persulfate can be activated by Cu-based catalysts via various pathways such as radical pathways (i.e., $\bullet\text{OH}$, $\bullet\text{SO}_4$) and non-radical pathways (i.e., $^1\text{O}_2$, surface complex). In the Cu-based non-radical persulfate activation pathway, the CuO and Cu_2O heterojunction catalysts could activate PDS or PMS on their surface to generate the active complexes [26,27]. For the Cu-based radical activation pathways, constructing copper-based heterojunctions could promote the Cu(II)/Cu(I) cycling, which is crucial for the formation of $\bullet\text{SO}_4$ and $\bullet\text{OH}$. Therefore, the in-depth investigation of selective conversion between radical and non-radical PDS/PMS activation pathways on Cu-based heterojunction is of great importance. Herein, we have successfully developed a $\text{Cu}_2\text{O}/\text{BiVO}_4$ heterostructure (Cu-BVO) for highly efficient organic pollutants degradation via PDS activation either in dark or upon light irradiation. More importantly, the Cu-BVO heterostructure could trigger the radical and non-radical PDS activation pathway under dark and light irradiation, respectively. Moreover, the radical/non-radical process of PDS activation and the relationship between the intrinsic active sites of the catalytic system and the PDS activation pathway was systematically elucidated through electron paramagnetic resonance (EPR) spectra, in-situ Raman spectra, photochemical behavior analysis and TDDFT calculations, with the goal of understanding and clarifying the switching of radical and non-radical pathways via light "on-off" over Cu-BVO heterostructures.

2. Materials and Methods

2.1. Synthesis of $\text{Cu}_2\text{O}/\text{BiVO}_4$ heterojunction

Firstly, 2.91 g $\text{Bi}(\text{NO}_3)_3 \cdot 5 \text{H}_2\text{O}$ was added into 30 mL HNO_3 (1 M) solution, and then 0.702 g NH_4VO_3 was also added to form homogenous solution under the sonication. The mixed solution was stirred for 2 h and then aged at a constant temperature of 70 °C for 15 h. After cooling down to room temperature, the sample was collected and washed with the deionized water for 5 times and finally dried at 60 °C for 12 h in a vacuum drying oven, which was denoted as BVO. Then, 0.5 g prepared BVO sample and 0.3775 g $\text{Cu}(\text{NO}_3)_2 \cdot 3 \text{H}_2\text{O}$ (Cu:Bi=20 wt%) were added into 50 mL deionized water to form a homogeneous solution. 50 mL of NaBH_4 (40 mM) was evenly dropped into the mixed solution with vigorous stirring under an ice-water bath. The final product was collected and washed with the deionized water for 5 times and finally dried at 60 °C for 12 h in a vacuum drying oven, which was denoted as Cu-BVO (10 wt%). A series of Cu-BVO nanocomposites with different Cu:Bi ratios (2.5, 5 and 20 wt%) were synthesized by varying the addition amount of $\text{Cu}(\text{NO}_3)_2 \cdot 3 \text{H}_2\text{O}$, respectively.

2.2. Catalytic performance evaluation

The photocatalytic experiments were performed by using a 300 W Xenon lamp of CEAu-Light (Vis, $\lambda \geq 420 \text{ nm}$) as the light source and the reaction temperature was fixed at 20 °C via a cooling water device. In the typical experiment, 30 mg of the catalyst was added into 30 mL of 20 mg L^{-1} bisphenol A (BPA) solution under magnetically stirring for 30 min in dark to achieve the adsorption-desorption equilibrium. Then 1 mL of PDS solution (90 mM) was added upon the light irradiation to perform the photocatalytic reaction. 2 mL of the suspension was sampled at each given time interval and filtered through a 0.22 μm syringe (Aqueous polyethersulfone filter). The concentration variation of BPA was monitored by high performance liquid chromatography (HPLC, Agilent 1260). The PDS concentration during the reaction was measured by adding 10 mL mixed solution of KHCO_3 and KI (1.5 g $\text{KHCO}_3 + 10 \text{ g KI}$ dissolved in 250 mL deionized water) into 250 μL the sample solution under a shaker for 30 min (25 °C, 180 r/min) via a UV-Vis spectrophotometer absorbance at 350 nm. The hydrogen peroxide was analyzed at 551 nm through the POD-catalyzed oxidation of DPD [28].

2.3. Details of theoretical calculations

In this work, we use first-principles excited states molecular dynamics methods with CP2K/Quickstep to study the collision [29], excitation and charge transfer processes of between molecules and interface. Molecular dynamics algorithm combined with NVT ensemble, Nose-Hoover thermostat [30], 1 fs step size, 500,000 steps. The force and velocity are calculated using time dependent density functional theory (TD-DFT) [31] for B3LYP functional [32], Gaussian-type basis set [33] and Goedecker-Teter-Hutter (GTH) pseudopotentials [34,35] combined with Gamma k-point and 400 eV cut-off energy. In the calculation steps, the energy minimization is used to balance the system, and then the Maxwell distribution method is used to give the molecules different collision probabilities, and then the dynamic process is conducted. The post processes analysis is performed by self-programs in Python. The isosurface maps of various orbitals and real space functions were rendered by means of Visual Molecular Dynamics (VMD) software based on the files exported by Multiwfn [32,36,37].

3. Results and discussion

3.1. Characterization of the Cu-BVO catalysts

The Cu-BVO nanocomposites are successfully prepared via a facile solution method (see Experimental Section, [Supplementary](#)

Information). The overall synthesis scheme for Cu-BVO is illustrated in Fig. 1a. According to the XRD pattern in Fig. 1b, the characteristic diffraction peaks of Cu-BVO phase structures correspond to cubic Cu_2O (PDF card no. 00-005-0667) and monoclinic BiVO_4 (PDF card no. 01-075-1866), respectively. As shown in TEM and SEM images (Figs. 1c and 1d), the granular Cu_2O with diameter of 10 nm are randomly dispersed on the surface of bulky BiVO_4 . HRTEM demonstrated an obvious contact surface between the two phases in the Cu-BVO composite with the staggered lattice fringes (Fig. 1e). The lattice fringe spacing of 0.256 nm denotes the (200) planes of the monoclinic BiVO_4 , and the 0.147 nm lattice fringe spacing is attributed to the (220) facets of Cu_2O (Fig. 1f). The corresponding fast Fourier transform pattern (FFT) further illustrated that Cu_2O covered the BiVO_4 basal plane along the [021] zone axis of BiVO_4 . In addition, we further validate the distribution of Cu and Bi/V on Cu-BVO by using energy dispersive X-ray spectroscopy (EDX) mapping (Fig. 1g) and line scan techniques (Fig. S1, Supporting Information). The uniform distribution of Cu, Bi, and V elements in Cu-BVO and the distinct interface of the heterostructures are clearly observed. The above experimental results indicate that the Cu-BVO heterojunction has been successfully synthesized.

3.2. Evaluation of PDS activation performance of Cu-BVO under dark and light

The $\text{Cu}_2\text{O}/\text{BiVO}_4$ heterostructure displays remarkable degradation efficiency for bisphenol A (BPA) via PDS activation. Fig. 2a shows the

time-dependent BPA degradation efficiency over Cu-BVO (10 wt%) sample under different conditions. The self-degradation of BPA and the direct degradation of BPA via PDS activation alone were found to be negligible. The degradation of BPA via PDS activation upon visible light irradiation is also poor, indicating that visible light cannot directly activate the PDS. Moreover, the degradation rate of BPA over Cu-BVO catalyst is less than 20% under visible light irradiation. However, the degradation rate of BPA reached 100% within 30 min after the introduction of PDS into the Cu-BVO/Vis reaction system. Interestingly, the BPA removal rate over the Cu-BVO/PDS system also reaches 100% in the absence of visible light, demonstrating that Cu-BVO could also efficiently activate the PDS to degrade BPA in dark. Fig. 2b shows the BPA degradation activity over single-component BiVO_4 and Cu_2O , respectively, under the same experimental conditions. The BPA removal rates on BiVO_4 and Cu_2O are found to be less than 20% both under visible light irradiation and in dark, illustrating that single-component BiVO_4 and Cu_2O are also unable to activate the PDS. In the reported literature, transition metal ions such as Fe^{2+} and Cu^{2+} could activate PDS through spontaneous electron transfer from a low valence state to a high valence state [38–40]. In order to exclude the effect of the released copper ion in the solution, relevant experiments are designed, and the result reveals that presented Cu^{2+} ions could not activate PDS to degrade BPA upon visible light irradiation or in dark (Fig. 2b).

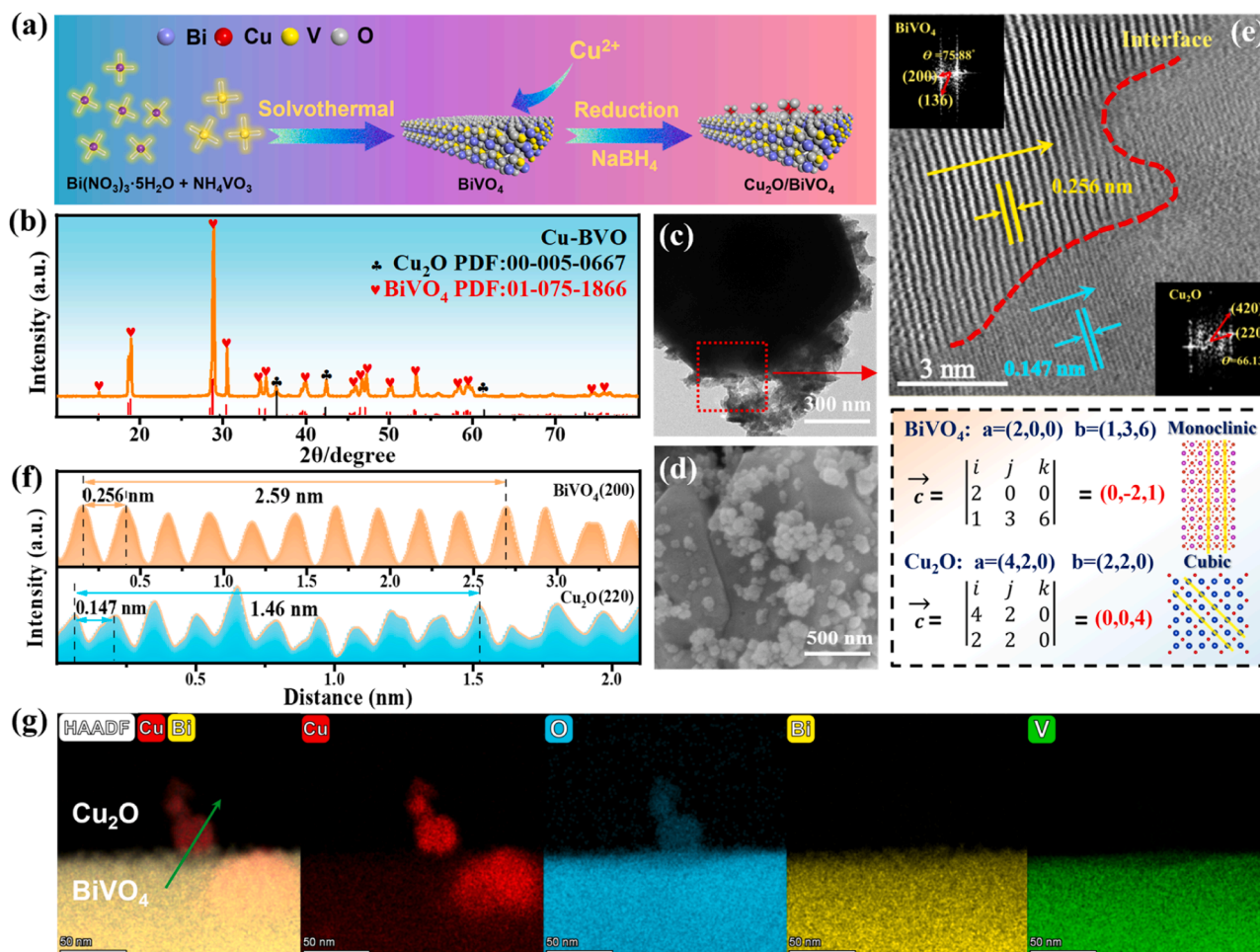


Fig. 1. Illustration scheme of the $\text{Cu}_2\text{O}/\text{BiVO}_4$ synthetic process (a). XRD pattern (b), TEM (c), SEM (d), HRTEM image and the corresponding fast Fourier transform (FFT) patterns of both sides of interface (e) of $\text{Cu}_2\text{O}/\text{BiVO}_4$ heterostructure. Lattice spacing obtained from the line intensity profiles taken along the yellow and cyan line shown in Fig. 1e (f). HAADF-STEM image and the corresponding elemental mappings of $\text{Cu}_2\text{O}/\text{BiVO}_4$ (g).

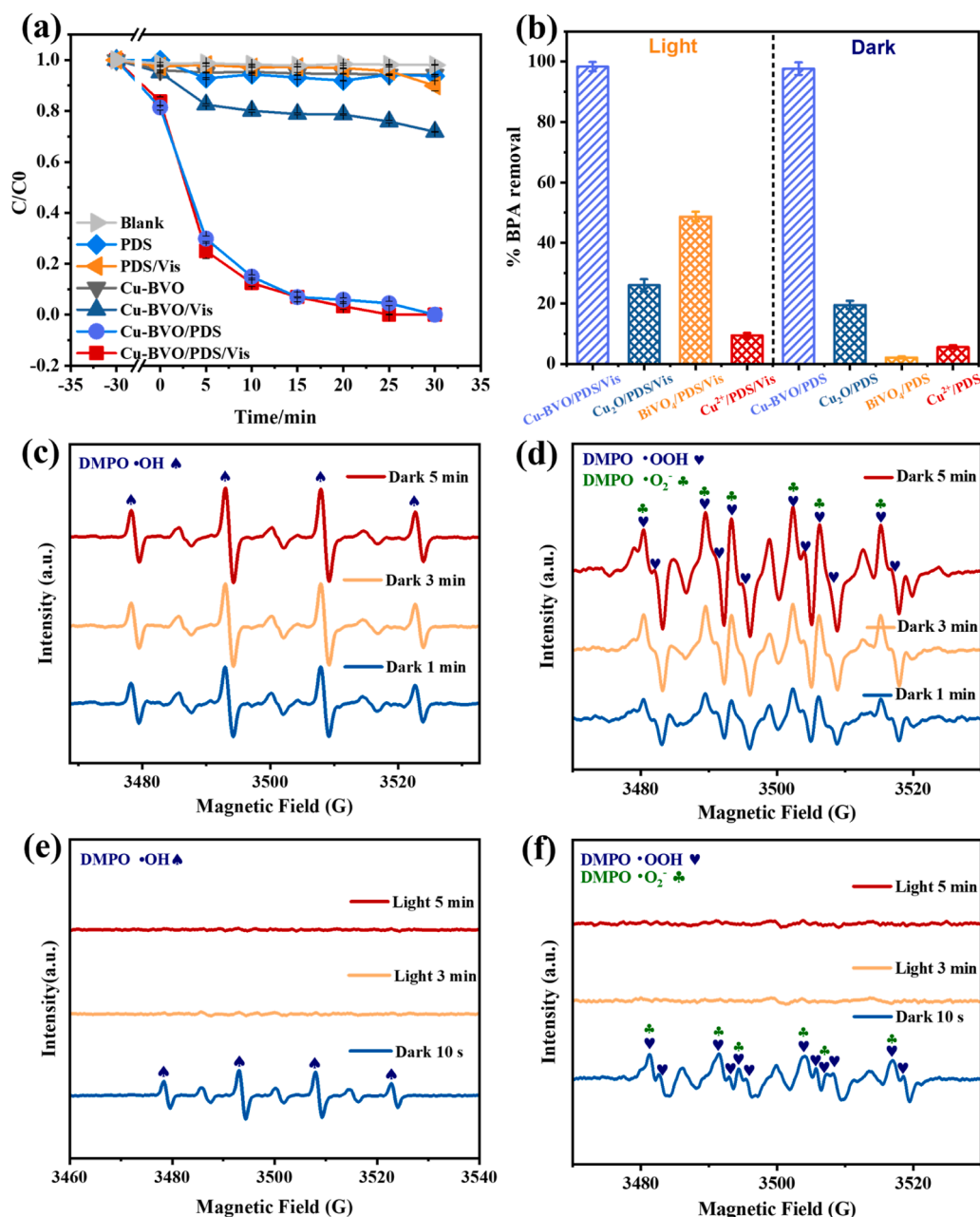


Fig. 2. Degradation of BPA under different conditions (a). Degradation efficiency of BPA over Cu-BVO, Cu₂O, BiVO₄, and Cu²⁺ in the presence of PDS in dark and upon light irradiation, respectively (b). EPR spectra of DMPO-•OH (c and e) and DMPO-•O₂⁻ (d and f) over Cu-BVO/PDS system in dark and upon light irradiation, respectively.

3.3. Identifying and distributions of reactive oxygen species

To identify the dominant active species generated in the Cu-BVO/PDS and Cu-BVO/PDS/Vis systems, the EPR characterization is performed as a direct monitor by using the DMPO as a trapping agent. In dark condition, the characteristic quartet signals with an obvious intensity ratio of 1:2:2:1 are detected, which is the single-electron signal of •OH ($a=14.79$, $g=2.006$), and the signal intensity gradually increases with the reaction time (Fig. 2c). The single-electron signals of •O₂⁻ are also revealed in the EPR spectra and gradually enhances with the prolongation of reaction time (Fig. 2d). The presence of slight •OOH signal is ascribed to the reaction of trace H₂O with •O₂⁻. However, the EPR signals of •OH and •O₂⁻ would disappear once upon visible light Controlled irradiation in the Cu-BVO/PDS system (Figs. 2e and 2f). No signal is detected in EPR spectra in the presence of individual Cu-BVO

and PDS, respectively (Fig. S2, Supplementary Information). In addition, to further confirm the role of the generated ROS in the BPA degradation, radicals trapping experiments are performed in dark and under visible light irradiation, respectively. As shown in Fig. S3a (Supplementary Information), the degradation of BPA over Cu-BVO via PDS activation in dark is significantly inhibited after adding the different scavengers of radicals (TBA, MeOH and BQ), respectively. Notably, only 40% of BPA degradation was inhibited upon the addition of TBA. We believe that the production of •SO₄ radicals occurs during the photocatalysis due to the obviously different reaction rate of TBA with •OH and •SO₄ ($k_{(•OH)} = 3.8-7.6 \times 10^8 \text{ M}^{-1}\text{s}^{-1}$, $k_{(•SO_4)} = 4-9.1 \times 10^5 \text{ M}^{-1}\text{s}^{-1}$) [7,41]. However, according to the reported literature, the generated •SO₄ could be converted to •OH in the presence of OH⁻, and therefore, no •SO₄ signal was detected in the EPR spectra [4]. The trapping experiments illustrate the production of •OH, •SO₄ and •O₂

radicals in dark conditions. Nevertheless, the effect of the scavengers on the degradation of BPA is negligible in the Cu-BVO/PDS/Vis system (Fig. S3b, Supplementary Information), indicating that no radicals is generated under visible light irradiation, which is in accord with the EPR measurement. The results indicate that dark activation and light activation may follow two different mechanisms: dark activation is a radical-involved process and light activation is a non-radical pathway.

Subsequently, in-situ EPR is performed to verify the transition of the radical to non-radical processes from dark to light conditions. Interestingly, a strong $\bullet\text{OH}$ signal appears under dark condition within 5 min, and the signal decreases significantly after lighting on for another 5 min. Finally, the strong $\bullet\text{OH}$ signal recovers again after lighting off for 5 min (Fig. 3a). The trend of the number of unpaired electron spins in each regular interval is also calculated by quadratic integration, as shown in Fig. 3b. It is further confirmed that the activation mechanism of PDS can be switched from radical process to non-radical process by light on-off. Moreover, the degradation of different kinds of pollutants (2,4 dichlorophenol (DCP), atrazine (ATZ), carbamazepine (CBZ)) is also investigated under dark and light activation conditions. It is found that the degradation rate of BPA and DCP reach 100% within 30 min under the dark activation system, while the degradation rate of ATZ and CBZ are less than 20% (Fig. 3c). However, all contaminants can be fully degraded within 30 min by PDS activation upon visible light irradiation. In summary, differences in dark/light activation mechanisms enable selectivity against different organic contaminants. In addition, the durability of Cu-BVO sample is also tested by recycling experiments for BPA photodegradation under light and dark activation systems, as depicted in Fig. S4 (Supplementary Information). No significant performance change is observed after 5-cycles experiments and no variation in the XRD pattern of Cu-BVO after 5-cycles, implying the good stability of Cu-BVO (Fig. S5, Supplementary Information). The results not only further confirm the different activation pathways of PDS under light

irradiation and under dark conditions, but also indicate promising applications of Cu-BVO/PDS and Cu-BVO/PDS/Vis systems for complex wastewater treatment.

3.4. Dark activation mechanism analysis

To understand the radical activation pathway in dark over Cu-BVO/PDS system, we employ XPS spectra to characterize the surface compositions and structures of Cu-BVO before and after dark activation (Fig. S6, Supplementary Information). The high-resolution XPS spectra of Bi 4f (Fig. 4a) of the Cu-BVO sample before PDS activation could be assigned to Bi^{3+} (158.67 and 163.80 eV) and $\text{Bi}^{(3+x)+}$ (159.51 and 164.90 eV). After dark activation, the peak intensity ratio of $\text{Bi}^{(3+x)+}/\text{Bi}^{3+}$ evidently increases, indicative of the transformation of Bi^{3+} to $\text{Bi}^{(3+x)+}$ during the degradation. While the proportion of Cu^+ (932.11 and 952.0 eV) in Cu-BVO decreases after the reaction, and the peaks of Cu^{2+} species (934.18 and 954.20 eV) together with its satellite peaks (943.20 and 962.80 eV) are detected, as shown in Cu 2p high-resolution spectra (Fig. 4b). The asymmetrical O 1s signal could be assigned to the lattice oxygen in BiVO_4 (O1, 529.80 eV), lattice oxygen in Cu_2O (O2, 531.40 eV) and the absorption oxygen (O3, 533.50 eV) before reaction, respectively (Fig. 4c). After the reaction, the peak of the lattice oxygen in Cu_2O (O2) obviously shifts to the high binding energy (532.20 eV), which is ascribed to the decrease of the electron cloud density in the surrounding environment of Cu-O, while no change is found in lattice oxygen (Bi-O) in BiVO_4 . This indicates that electrons in Cu_2O migrate to the PDS molecule, leading to dark activation of the PDS and the generation of reactive oxygen species. Therefore, it is proposed that Cu(I) species of Cu_2O act as an initiator to activate PDS (R1) and subsequently result in the production of hydroxide radicals (R2), and the fluorescence intensity of 7-hydroxycoumarin at 425 nm in the coumarin fluorescent probe experiment increases with the reaction time, which further

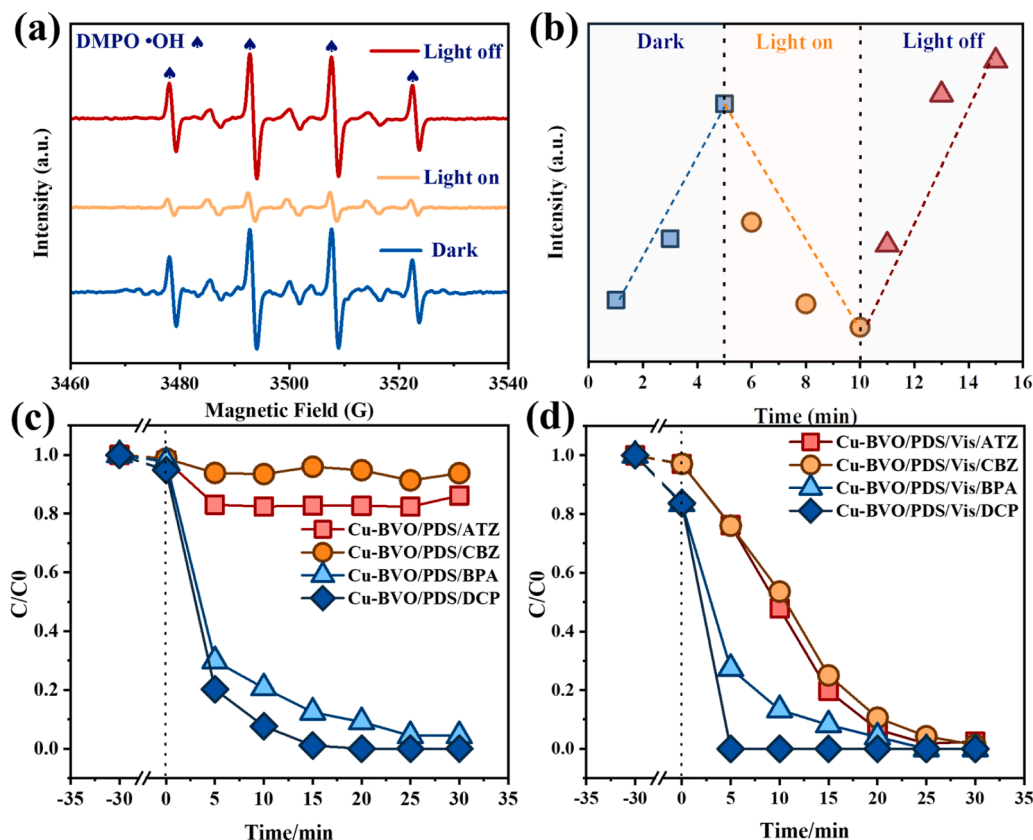


Fig. 3. EPR spectra (a) and time-dependent intensity (b) of DMPO- $\bullet\text{OH}$ over Cu-BVO/PDS under continuous dark-light-dark condition. Degradation of ATZ, CBZ, BPA, DCP over Cu-BVO/PDS system in dark (c) and upon light irradiation (d).

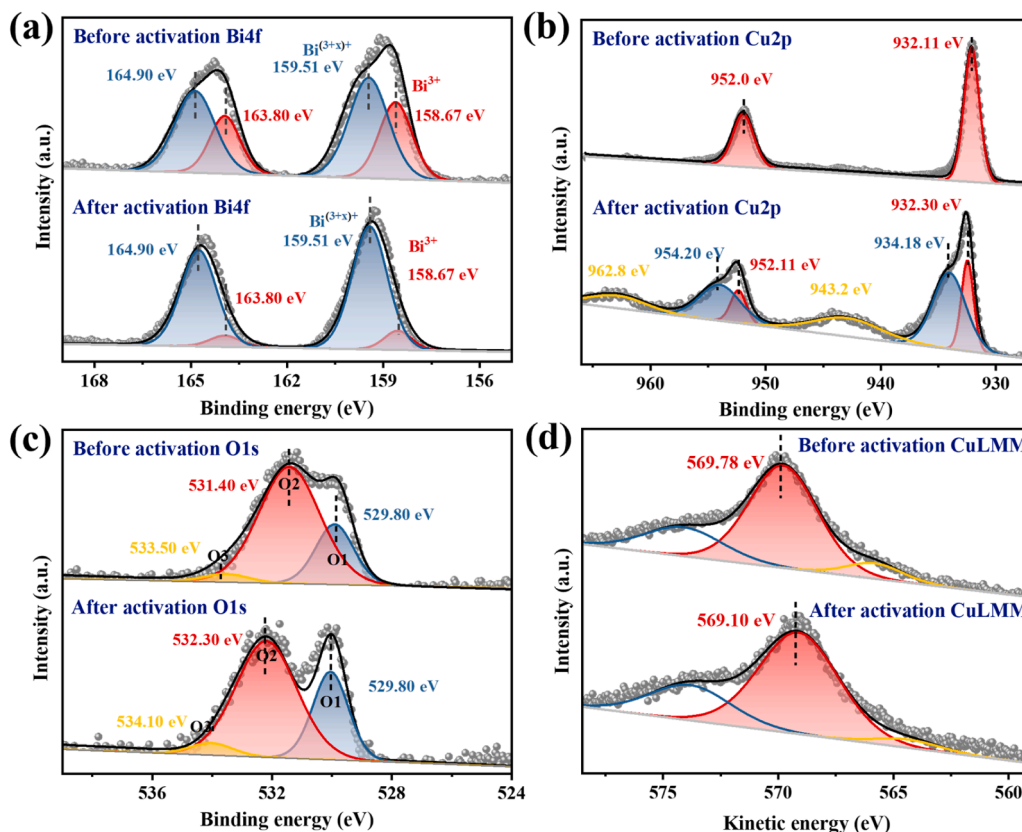


Fig. 4. High-resolution XPS spectra of Bi 4 f (a), Cu 2p (b), O1s (c) and Cu LMM auger electron spectra (d) of Cu-BVO before and after PDS activation in dark.

verifies that $\bullet\text{OH}$ content gradually increases (Fig. S8, Supplementary Information). Cu(I) species also might have potential to react with O_2 via the single electron transfer to generate superoxide radicals ($\text{R}3$), and then further react to generate $\bullet\text{O}_2\text{H}$, which also matches well with the changes of EPR signal. However, it should be noted that the actual response system may involve additional complexities. For instance, the contact interface between semiconductor material and solution may generate a space-charge layer, resulting in a shift of the semiconductor Fermi level. The generation of $\text{Bi}^{(3+x)+}$ indicates that electron transfer occurred between $\text{Bi}^{3+}/\text{Bi}^{(3+x)+}$ and $\text{Cu}^+/\text{Cu}^{2+}$ during the reaction (R4). The generated hydroxide radicals and superoxide radicals also simultaneously lead to the production of hydrogen peroxide ($\text{R}5\sim\text{R}7$), which is detected in the reaction solution by DPD chromogenic method [28, 42]. It is observed that the H_2O_2 is produced during the reaction, and the concentration of H_2O_2 increases slowly with prolonging the reaction time, as shown in Fig. S9 (Supplementary Information). We find that H_2O_2 is a key intermediate to generate $\bullet\text{O}_2$ and promote electron cycling of $\text{Bi}^{3+}/\text{Bi}^{(3+x)+}$ and $\text{Cu}^+/\text{Cu}^{2+}$. Based on the above discussions, the potential reaction pathway involved in PDS activation are summarized in Scheme S1 (Supplementary Information).

Up to date, three mainstream non-radical pathways have been extensively reported, including singlet oxygenation, electron-transfer processes (ETP), and high valent metal induced oxidation [4,43]. EPR analysis is performed with TEMP to trap $^1\text{O}_2$ to produce 2,2,6,6-tetramethylpiperidine-N-oxyl (TEMPO), recognized by the characteristic triplet signals with the intensity ratio of 1:1:1. Although the characteristic triplet signals with the intensity ratio of 1:1:1 are detected in the EPR spectra both in dark and under visible light irradiation (Fig. S10a, Supplementary Information), the intensity of EPR signal does not alter when the EPR measurements are performed in deuterium oxide (D_2O) solution (Fig. S10b, Supplementary Information). As we know, there are many possible pathways to generate this signal [44,45]. Hence, it illustrates that the signal is not generated by the reaction of $^1\text{O}_2$ with

TEMP due to the different lifetime of $^1\text{O}_2$ in D_2O ($\tau_{1/2} = 20\sim 32\ \mu\text{s}$) and H_2O ($\tau_{1/2} = 2\ \mu\text{s}$) [46]. In addition, the use of D_2O slows down the overall dynamics of aqueous reactions, such that if oxidation is accelerated in D_2O , the reaction may involve singlet oxygen. We further test the degradation performance of BPA by Cu-BVO/PDS/Vis systems in D_2O and H_2O , and the results show that no significant change in BPA degradation efficiency is found in different solvents (Fig. S10c, Supplementary Information). It illustrates that the singlet oxygen does not participate in the photoactivation process. Based on the above experimental results, the degradation process of Cu-BVO/PDS/Vis system is not dominated by singlet oxygenation, so we conclude that ETP plays a leading role in the photoactivation process [4,47].

3.5. Interaction between Cu-BVO and PDS in light/darkness

To further explore the interaction mode between catalyst and PDS, the dynamics of PDS consumption were investigated. As illustrated in Fig. S12, in the dark activation system, the consumption of PDS increases with the increase of catalyst and BPA concentration (approximate first-order reaction for catalyst and BPA, respectively), indicating that the dark activation process predominantly relies on the participation of free radicals presented in the solution. Differently, PDS consumption under irradiation only depends on the catalyst concentration and almost unchanged with the increase of BPA concentration. It illustrates that the photoactivation pathway is significantly different from the radical pathway in dark condition. The photoactivation is more relied on the surface interaction of PDS with the catalyst. ETP can further be categorized into two processes via inner-sphere or outer-sphere oxidation, depending on the interaction behaviors of the reactants (organic and persulfate) with the catalyst. The complexation mode of PDS in the Cu-BVO/Vis system is investigated by varying the ionic strength of the solution. The degradation of BPA in the Cu-BVO/PDS/Vis system gradually decreases with the increase of ionic

strength, illustrating that the increase of ionic strength inhibit the electrostatic interactions between the PDS molecules and catalyst nanoparticles (Fig. S13, Supplementary Information). Otherwise, the increase of ionic strength would have no influence on BPA degradation, because the increase of ionic strength does not influence on the inner complexation (Covalent bonding) between the nanoparticles surface and the solute. Moreover, attenuated total reflection Fourier transform infrared spectroscopy (ATR-FTIR) show that there is no new covalent bond between Cu-BVO and PDS, further confirm that the interaction between the Cu-BVO and PDS occurs through the outer surface complexation (Fig. S14, Supplementary Information).

Subsequently, in-situ Raman spectroscopy is performed to probe the chemical evolution of catalyst-persulfate (Cat-PDS*) complexes under visible light irradiation. As shown in Fig. 5a, the peaks at 836 and 1075 cm^{-1} correspond to the characteristic peaks of the S-O and S=O stretching vibrations in PDS, respectively [48,49]. With prolonging the illumination time, the Raman scattering intensity of the characteristic shoulder peak ascribed to O-O bending vibration at 802 cm^{-1} gradually enhances, and the peak area ratio of (O-O)/(S-O) increased from 1.18 to 2.28 (Fig. 5b) [50,51]. However, no other significant change and new signal peak is observed in the Raman spectra of Cu-BVO in Cu-BVO/PDS/Vis system (Fig. 5c). Also, the signal intensity of PDS alone does not change significantly after illumination (Fig. S15). It indicates that the O-O bond polarization of PDS adsorbed on the Cu-BVO surface increases under photoexcitation and promotes the production of sub-stable Cat-PDS*, of which the activated PDS intermediate will eventually decompose directly to SO_4^{2-} (982 cm^{-1}) [14,52,53]. In order to further explore the kinetic process of PDS on the catalyst surface at the molecular scale, we utilize Time-Dependent Density Functional Theory (TDDFT) to simulate the dynamic structure evolution of O-O bonds of PDS molecules after photoexcitation [36,54]. Following

photoexcitation, we find that the O-O bond length increases from 1.467 Å to 2.418 Å at 1000 fs (Fig. 5d). In addition, the dipole moments of the ground and excited singlet states also have been calculated using DFT/TDDFT. Compared with the ground state dipole moment ($\mu_g=4.23$ D), the excited state dipole moment ($\mu_e=6.35$ D) of PDS under photoexcitation increases by 2.12 D, and the direction of excited state dipole moment is from PDS (positive electricity center) to catalyst (negative electricity center), as shown in Fig. 5e. It is the difference in the charge distribution between the PDS and the catalyst that causes the change in the dipole moments of the ground and excited states. The above experimental results indicate that the electron density of PDS decreases after photoexcitation (The photogenerated hole occupied bonding O2p bands of the O-O), and a force to stretch the O-O bond is generated due to the empties of the O-O bonding state, and then generates a metastable Cat-PDS* and elevate the overall redox potential of the catalyst (E_{cat}).

3.6. Photogenerated electron-hole dynamics analysis

To further elucidate the migration of photogenerated carriers in Cu-BVO sample, the UV-Vis diffuse reflectance spectra of the corresponding Cu_2O and BiVO_4 are performed, as shown in Fig. S16a (Supplementary Information). The forbidden band width (E_g) of Cu_2O and BiVO_4 are calculated to be 1.96 and 2.38 eV, based on the Kubelka-Munk formula: $ah\nu=A(h\nu-E_g)^{1/2}$, respectively. The valence band edge potentials (E_{VB}) of Cu_2O and BiVO_4 are also determined to be 1.84 and 2.78 V (relative to the standard hydrogen electrode) by VB-XPS from the formula of E_{VB} , $\text{NHE}=\phi+E_{\text{VB}}$, $\text{XPS}+0.0592 \cdot \text{pH}$ (Fig. S16b, Supplementary Information). Then the corresponding conduction band (E_{CB}) potentials are calculated to be -0.12 and 0.4 eV by the empirical formula ($E_g=E_{\text{VB}}-E_{\text{CB}}$). The DMPO-•OH and DMPO-•O₂ EPR spectra of Cu-BVO in dark and upon visible light irradiation (Fig. S17, Supplementary Information) reveal

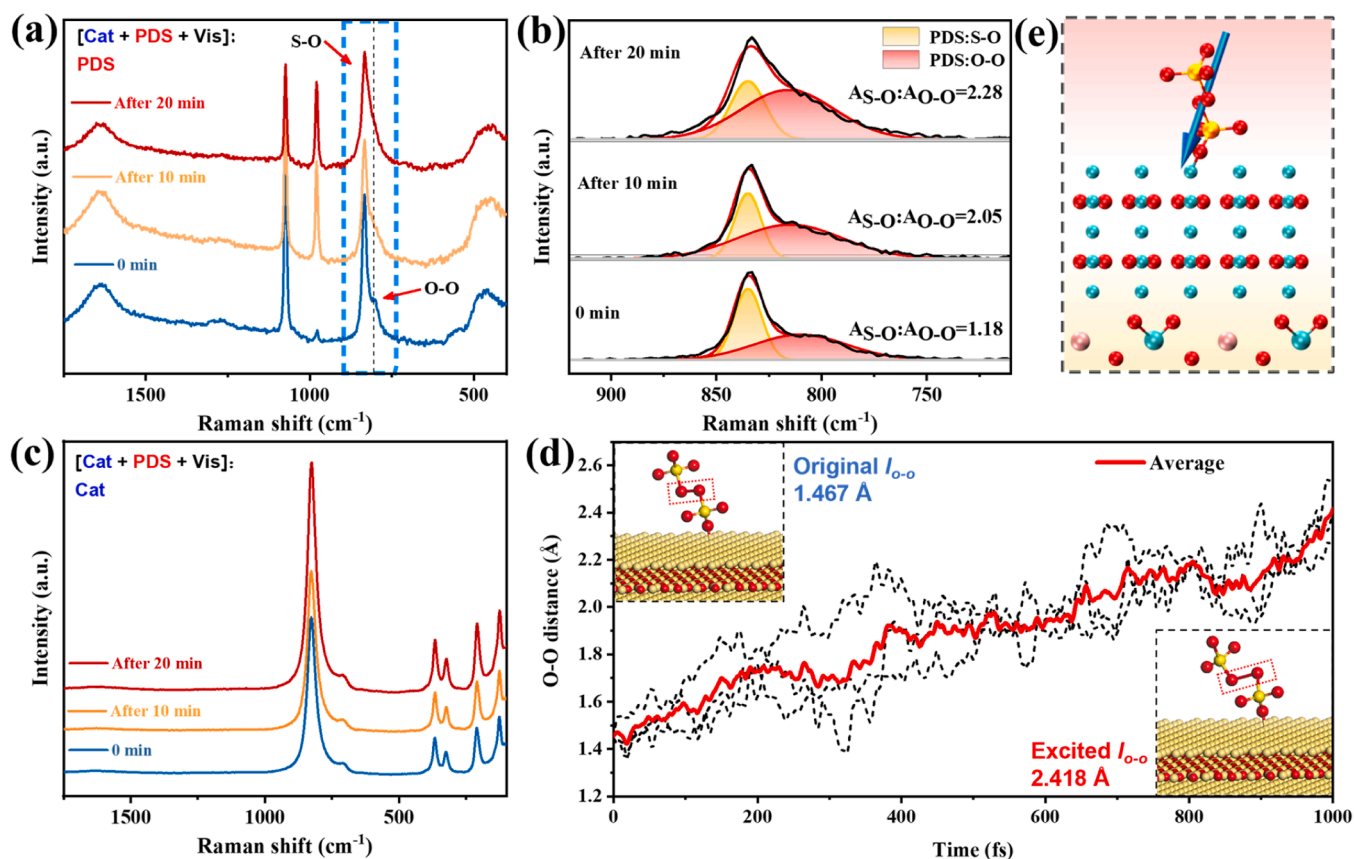


Fig. 5. Time-dependent Raman spectra of PDS (a), enlarged range of 650–950 cm^{-1} of Fig. 5a (b) and Cu-BVO (c) in Cu-BVO/PDS/Vis system. Dynamic evolution of O-O bonds in PDS within 1000 fs under photoexcitation (d). Depiction of the excited dipole moment direction of PDS using VMD (e).

that the reduction and oxidation capacities of both photogenerated electrons and holes are not sufficient to generate $\bullet\text{O}_2$ and $\bullet\text{OH}$. Moreover, according to the band structure of Cu-BVO, the photo-generated electrons and the photo-generated holes should migrate to the BiVO_4 and the Cu_2O under light excitation, respectively. Therefore, it is considered that the carrier migration modes in the Cu-BVO composite material under photoexcitation belong to the characteristics of Type-II photocatalytic process, instead of Z-scheme pathway, as illustrated in Fig. S18a (Supplementary Information).

It is well known that the surface chemical properties of excited catalysts largely determine the activation pathways and catalytic activity of persulfate. In order to further investigate the influence of real photo-activation Cu-BVO charge distribution on the activation of PDS, the natural orbital transition analysis (NTO) from the ground state (S_0) to first excited singlet state (S_1) of the Cu-BVO is performed, and the contributions of molecular orbitals to electron and holes are quantitatively studied to determine the reactivity origin of Cu-BVO system [1]. The photoexcited electrons and holes mainly come from the highest occupied molecular orbital (HOMO) and the lowest unoccupied molecular orbital (LUMO), and the calculated contributions are 69.34% and 71.11%, respectively (Table S1, Supplementary Information). Hence, we could characterize electron excitation qualitatively by analyzing HOMO and LUMO orbitals [55]. The HOMO-LUMO analysis is implemented on the excited states by using TDDFT calculations. After photoexcitation, HOMO is mainly on the Cu atom of Cu_2O , while the LUMO is localized partly on the V and Bi atoms of BiVO_4 (Fig. 6a). From the atomic contribution point of view, both electrons and holes possess significant delocalization characteristics. A comprehensive analysis of the hole-electron distribution of the dominant excitation processes in Cu-BVO has been performed based on TDDFT simulations. Hole-electron analysis describes the electron excitation in a molecule as a process of electron transfer from 'hole' area to 'electron' area, and visually examined the excitation characteristics of excited electrons [37,56]. The basic analytical results regarding the hole-electron distribution are listed in

Table S2. It can be found that the degree of overlap between electrons and holes in the Cu-BVO structure is low, and the electron-hole center of mass distance (D) gradually increases after photoexcitation. After about 500 fs, the electron-hole distance arrives at a stable value of 7 Å (Fig. S19). From the t-index, the t-index of $S_0 \rightarrow S_1$ is positive (3.91), which indicates an obvious hole and electron separation. It is therefore reasonable to conclude that the excitation mode of $S_0 \rightarrow S_1$ is charge transfer excitation (CT). In general, the possibility of hole-electron pair recombination is low, which favors charge conduction between the PDS and the catalyst. At the same time, the hole delocalization degree of PDS/Cu-BVO system (HDI=15.53) is significantly higher than that of Cu-BVO system (HDI=8.37), which indicates the migration of holes to PDS to a certain extent. Fig. 6b shows the real-space charge distribution of electrons and holes on the Cu-BVO. It is observed that electrons and holes are enriched in BiVO_4 and Cu_2O , respectively, during the photoexcitation process, which is also in agreement with our analysis based on the band structure. Therefore, the electron-deficient region formed on the surface of Cu_2O is more thermodynamically conducive to the accumulation of PDS, providing a more suitable platform for the generation of the metastable surface restricted activation PDS complex (Cat-PDS*). To verify this speculation, the influence of the addition of hole quencher (TEOA) on the degradation of BPA is also investigated. It is found that the addition of TEOA could significantly inhibit the BPA degradation, further illustrating that photogenerated holes play a key role in the activation of PDS (Fig. S21, Supplementary Information).

3.7. Electron migration analysis between Cu-BVO and PDS

The charge transfer and separation behavior between PDS and Cu-BVO is also adequately demonstrated by in-situ X-ray photoelectron spectroscopy (XPS). Under dark conditions, the peak of the signal corresponding to Cu^+ in Cu-BVO is shifted by 0.87 eV towards higher binding energy after the addition of PDS, indicating that electron migration from Cu-BVO to PDS occurs, resulting in a decrease in the

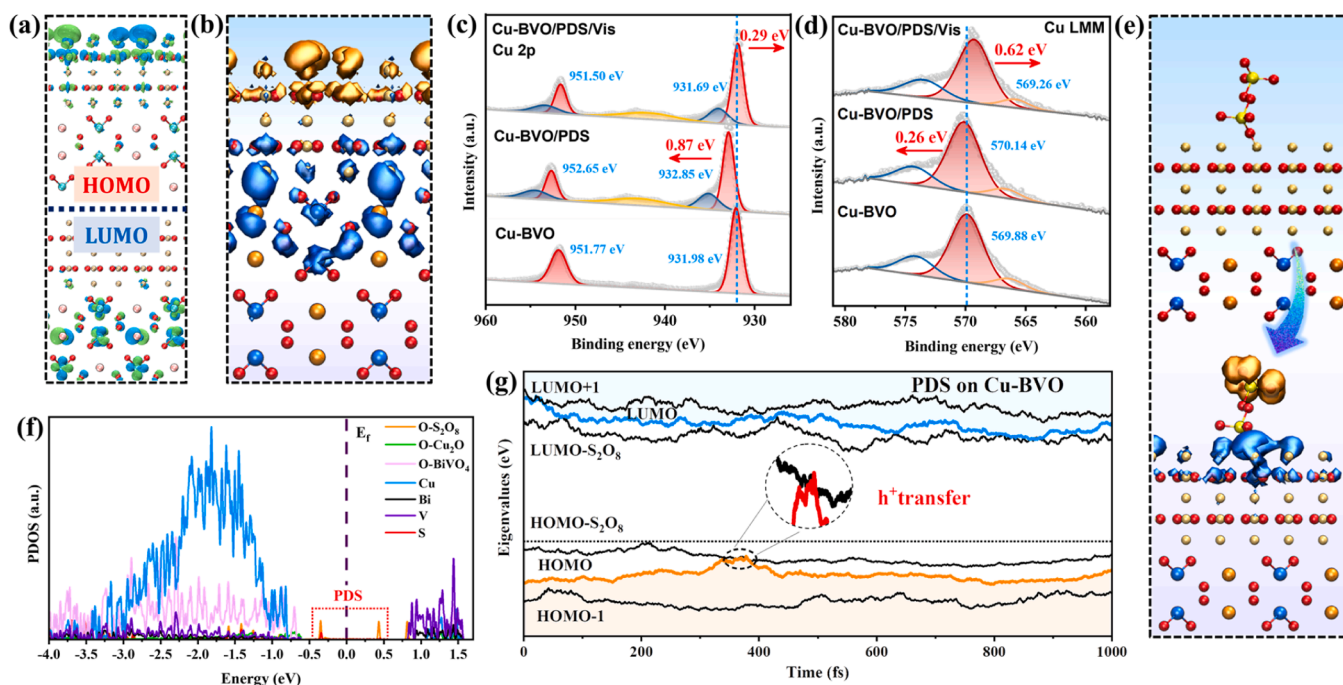


Fig. 6. The spatial distribution of HOMO/LUMO (excited state) of Cu-BVO obtained by TDDFT calculation (a). The blue and green represents the negative and positive phases of molecular orbitals, respectively. Real space representation of hole (yellow) and electron (blue) distributions of the Cu-BVO under $S_0 \rightarrow S_1$ excitation (b). In-situ XPS spectra of Cu2p in Cu-BVO (c) and Cu LMM auger electron spectra (d) under different conditions. Real space representation of hole (yellow) and electron (blue) distributions of the Cu-BVO/PDS system (e). Partial density of states (PDOS) of PDS adsorbed on Cu-BVO surface (f). Evolution of nonadiabatic state energy levels as functions of time in TDDFT simulations (g). The yellow and blue lines represent the time-dependent energy eigenvalues evolution corresponding to holes and hot electrons respectively.

electron cloud density around Cu-BVO. Subsequently, visible light is introduced into the detection vacuum chamber and the test is performed after 10 min. Interestingly, the signal peak corresponding to Cu^+ at this time is shifted by 0.29 eV toward the lower binding energy compared to the initial Cu^+ , indicating that the Cu-BVO accept electron from the PDS after light exposure and the electron flow is reversed (Fig. 6c). The same pattern is also shown in Cu LMM auger electron spectroscopy (Fig. 6d). The reversal of the electron flow between the PDS and the catalyst under photoexcitation also leads to a change in the activation mechanism of the PDS. In the absence of BPA, 65% of the PDS could be decomposed over the Cu-BVO composite within 30 min under visible light irradiation. However, the decomposition rate of PDS decrease significantly with the addition of BPA (Fig. S22, Supplementary Information), which is the opposite of the radical oxidation process, as the addition of contaminants would promote the decomposition of PDS in the case of a radical oxidation process. Therefore, we suggest that the metastable PDS^* generated during the photoactivation process directly capture electrons from BPA molecules, which decelerate the transfer rate of electrons from PDS to Cu-BVO and reduce the decomposition amount of PDS. In addition, TDDFT calculations have been used to investigate the influence of the electronic dynamical behavior of the PDS-material interface on the excitation state of the PDS under photoexcitation. Fig. 6e shows the distribution of electrons and holes in the PDS molecule in real space, indicating that electrons in the PDS migrate and accumulate on the Cu_2O surface after light exposure. Then, we calculate the partial density of states (PDOS) of Cu-BVO/PDS system based on DFT and analysis the energy level distribution of different MOs [31,57]. The results manifest that HOMO- S_2O_8 and LUMO- S_2O_8 local states are generated on both sides of CBM and VBM of the PDS molecules (Fig. 6f). Effective charge transfer during photoexcitation requires the highest occupied molecular orbital of the PDS to be close to the valence band of Cu_2O . Therefore, in the Cu-BVO/PDS system, we first activate an electron from the HOMO to the LUMO via perpendicular excitation, then the energy levels of the non-adiabatic eigenstates in the system are evolved by TDDFT (Fig. 6g). It could be found that at about 390–400 fs, the energy level corresponding to the hole produced by Cu_2O suddenly rises, attacking the electron bound state of PDS (HOMO- S_2O_8). Along with the intersection of these two energy levels, the photogenerated holes initially in the HOMO level is excited to the HOMO- S_2O_8 energy level, which indicates that the Cu-BVO system could pump electrons from the electron bound state of PDS into the conduction band of Cu_2O during the process of photoexcitation. Corresponding to the radicals change rule in the in-situ EPR described above, it can be found that the light acts as a switch to control the electron flow direction between PDS and the catalyst, realizing the controllable transition between radical activation and non-radical activation of PDS.

4. Conclusions

In summary, we have successfully fabricated a stable $\text{Cu}_2\text{O}/\text{BiVO}_4$ heterojunction (Cu-BVO) for highly efficient degradation of pollutants through PDS activation in both dark and light conditions. Notably, by modulating the light “on-off” state, we were able to control the electron flow direction between the PDS and Cu-BVO, enabling a transition from radical activation process to non-radical pathway. In the absence of light, Cu_2O acts as an electron donor to activate PDS through a one-electron reaction to generate $\bullet\text{OH}$ and $\bullet\text{O}_2$, while continuous PDS activation is achieved through redox cycling between $\text{Cu}^+/\text{Cu}^{2+}$ and $\text{Bi}^{3+}/\text{Bi}^{(3+x)+}$ species. Upon light irradiation, directional migration of photo-generated carriers in Cu-BVO creates an electron-deficient region on the surface of Cu_2O , promoting the generation of metastable intermediates (Cu-BVO/ PDS^*) by consuming electrons in PDS. These activated intermediates directly degrade organic pollutants without generating radicals. This work presents an example of controlled conversion of radical and non-radical PDS activations, and it also implements non-radical activation of PDS via photocatalytic assisted induction. Our

findings provide a novel approach to the selective regulation of the persulfate activation mechanism.

CRedit authorship contribution statement

Chen Rong: Supervision, Writing – review & editing. **Guo Sheng:** Data curation, Methodology. **Li Guangfang:** Data curation, Investigation. **Liu Qiong:** Software. **Guo Wenjin:** Formal analysis, Methodology. **Bai Chengbo:** Data curation, Formal analysis, Investigation, Methodology, Writing – original draft.

Declaration of Competing Interest

The authors declare no competing financial interest.

Data Availability

Data will be made available on request.

Acknowledgements

This work was supported by the National Natural Science Foundation of China (22076149), the Innovative Team Program of Natural Science Foundation of Hubei Province (2023AFA027) and Special Project of State Key Laboratory of New Textile Materials & Advanced Processing Technologies from Wuhan Science and Technology Bureau (2022013988065204).

Appendix A. Supporting information

Supplementary data associated with this article can be found in the online version at doi:10.1016/j.apcatb.2023.123606.

References

- [1] F. Qin, E. Almatrafi, C. Zhang, D. Huang, L. Tang, A. Duan, D. Qin, H. Luo, C. Zhou, G. Zeng, Catalyst-free photochemical activation of peroxymonosulfate in xanthene-rich systems for Fenton-like synergistic decontamination: efficacy of proton transfer process, *Angew. Chem. Int. Ed.* 62 (2023), e202300256.
- [2] S. Liu, Y. Hu, H. Xu, Z. Lou, J. Chen, C.-Z. Yuan, X. Lv, X. Duan, S. Wang, X.-L. Wu, Directional electron transfer in single-atom cobalt nanozyme for enhanced photo-Fenton-like reaction, *Appl. Catal. B: Environ.* 335 (2023) 122882–122891.
- [3] D. Zhang, Y. Li, P. Wang, J. Qu, Y. Li, S. Zhan, Dynamic active-site induced by host-guest interactions boost the Fenton-like reaction for organic wastewater treatment, *Nat. Commun.* 14 (2023) 3538.
- [4] S. He, Y. Chen, X. Li, L. Zeng, M. Zhu, Heterogeneous photocatalytic activation of persulfate for the removal of organic contaminants in water: a critical review, *Acs. Est. Engg.* 2 (2022) 527–546.
- [5] F. Li, Z. Lu, T. Li, P. Zhang, C. Hu, Origin of the excellent activity and selectivity of a single-atom copper catalyst with unsaturated Cu-N₂ sites via peroxydisulfate activation: Cu(III) as a dominant oxidizing species, *Environ. Sci. Technol.* 56 (2022) 8765–8775.
- [6] Y. Yan, Z. Wei, X. Duan, M. Long, R. Spinney, D.D. Dionysiou, R. Xiao, P.J. Alvarez, Merits and limitations of radical vs. nonradical pathways in persulfate-based advanced oxidation processes, *Environ. Sci. Technol.* 57 (2023) 12153–12179.
- [7] A. Jawad, K. Zhan, H. Wang, A. Shahzad, Z. Zeng, J. Wang, X. Zhou, H. Ullah, Z. Chen, Z. Chen, Tuning of persulfate activation from a free radical to a nonradical pathway through the incorporation of non-redox magnesium oxide, *Environ. Sci. Technol.* 54 (2020) 2476–2488.
- [8] Y. Nosaka, A.Y. Nosaka, Generation and detection of reactive oxygen species in photocatalysis, *Chem. Rev.* 117 (2017) 11302–11336.
- [9] J. Liu, P. Wu, S. Yang, S. Rehman, Z. Ahmed, N. Zhu, Z. Dang, Z. Liu, A photo-switch for peroxydisulfate non-radical/radical activation over layered CuFe oxide: rational degradation pathway choice for pollutants, *Appl. Catal. B: Environ.* 261 (2020), 118232.
- [10] X. Duan, H. Sun, Z. Shao, S. Wang, Nonradical reactions in environmental remediation processes: uncertainty and challenges, *Appl. Catal. B: Environ.* 224 (2018) 973–982.
- [11] Y. Ding, X. Wang, L. Fu, X. Peng, C. Pan, Q. Mao, C. Wang, J. Yan, Nonradicals induced degradation of organic pollutants by peroxydisulfate (PDS) and peroxymonosulfate (PMS): recent advances and perspective, *Sci. Total. Environ.* 765 (2021) 142794–142815.
- [12] Y.-J. Zhang, G.-X. Huang, L.R. Winter, J.-J. Chen, L. Tian, S.-C. Mei, Z. Zhang, F. Chen, Z.-Y. Guo, R. Ji, Y.-Z. You, W.-W. Li, X.-W. Liu, H.-Q. Yu, M. Elimelech,

- Simultaneous nanocatalytic surface activation of pollutants and oxidants for highly efficient water decontamination, *Nat. Commun.* 13 (2022) 3005.
- [13] W. Ren, C. Cheng, P. Shao, X. Luo, H. Zhang, S. Wang, X. Duan, Origins of electron-transfer regime in persulfate-based nonradical oxidation processes, *Environ. Sci. Technol.* 56 (2022) 78–97.
 - [14] B. Wang, C. Cheng, M. Jin, J. He, H. Zhang, W. Ren, J. Li, D. Wang, Y. Li, A site distance effect induced by reactant molecule matchup in single-atom catalysts for Fenton-like reactions, *Angew. Chem. Int. Ed.* 61 (2022), e202207268.
 - [15] J.K. McCusker, Electronic structure in the transition metal block and its implications for light harvesting, *Science* 363 (2019) 484–488.
 - [16] J. Yang, M. Zhang, M. Chen, Y. Zhou, M. Zhu, Oxygen vacancies in piezoelectric ZnO twin-mesocrystal to improve peroxymonosulfate utilization efficiency via piezo-activation for antibiotic ornidazole removal, *Adv. Mater.* 35 (2023) 2209885.
 - [17] M. Zhang, X. Lin, Z. Yi, X. Xu, J. Yang, M. Zhu, Enhanced reactive oxidation species generation by ligand-to-metal-charge transfer between oxygen vacancy-rich ZnO mesocrystal with ciprofloxacin pollutants, *Appl. Catal. B: Environ.* 321 (2023), 122033.
 - [18] M. Zhang, H. Tao, C. Zhai, J. Yang, Y. Zhou, D. Xia, G. Comodi, M. Zhu, Twin-brush ZnO mesocrystal for the piezo-activation of peroxymonosulfate to remove ibuprofen in water: performance and mechanism, *Appl. Catal. B: Environ.* 326 (2023), 122399.
 - [19] X.L. Wu, S. Liu, M. Yan, H. Lin, J. Chen, S. Liu, S. Wang, X. Duan, Directional and ultrafast charge transfer in oxygen-vacancy-rich ZnO@single-atom cobalt core-shell junction for photo-Fenton-like reaction, *Angew. Chem. Int. Ed.* 62 (2023), e202305639.
 - [20] M. Qian, X.L. Wu, M. Lu, L. Huang, W. Li, H. Lin, J. Chen, S. Wang, X. Duan, Modulation of charge trapping by island-like single-atom cobalt catalyst for enhanced photo-Fenton-like reaction, *Adv. Funct. Mater.* 33 (2023) 2208688.
 - [21] B. Huang, X. Fu, K. Wang, L. Wang, H. Zhang, Z. Liu, B. Liu, J. Li, Chemically bonded BiVO₄/Bi₁₉Cl₃S₂₇ heterojunction with fast hole extraction dynamics for continuous CO₂ photoreduction, *Adv. Power Mater.* 5 (2023), 100140.
 - [22] C. Xu, P. Ravi Anusuyadevi, C. Aymonier, R. Luque, S. Marre, Nanostructured materials for photocatalysis, *Chem. Soc. Rev.* 48 (2019) 3868–3902.
 - [23] L.G. Kaake, J.J. Jasieniak, R.C. Bakus, G.C. Welch, D. Moses, G.C. Bazan, A. J. Heeger, Photoinduced charge generation in a molecular bulk heterojunction material, *J. Am. Chem. Soc.* 134 (2012) 19828–19838.
 - [24] M. Wang, J. Iocozia, L. Sun, C. Lin, Z. Lin, Inorganic-modified semiconductor TiO₂ nanotube arrays for photocatalysis, *Energy Environ. Sci.* 7 (2014) 2182–2202.
 - [25] H. Wang, W. Liu, X. He, P. Zhang, X. Zhang, Y. Xie, An excitonic perspective on low-dimensional semiconductors for photocatalysis, *J. Am. Chem. Soc.* 142 (2020) 14007–14022.
 - [26] H. Li, J. Tian, F. Xiao, R. Huang, S. Gao, F. Cui, S. Wang, X. Duan, Structure-dependent catalysis of cuprous oxides in peroxymonosulfate activation via nonradical pathway with a high oxidation capacity, *J. Hazard Mater.* 385 (2020), 121518.
 - [27] T. Zhang, Y. Chen, Y. Wang, J. Le Roux, Y. Yang, J.-P. Croué, Efficient peroxydisulfate activation process not relying on sulfate radical generation for water pollutant degradation, *Environ. Sci. Technol.* 48 (2014) 5868–5875.
 - [28] Z. Dai, F. Qin, H. Zhao, J. Ding, Y. Liu, R. Chen, Crystal defect engineering of Aurivillius Bi₂MoO₆ by Ce doping for increased reactive species production in photocatalysis, *ACS Catal.* 6 (2016) 3180–3192.
 - [29] K.-i. Ataka, T. Yotsuyanagi, M. Osawa, Potential-dependent reorientation of water molecules at an electrode/electrolyte interface studied by surface-enhanced infrared absorption spectroscopy, *J. Phys. Chem. C* 100 (1996) 4253–4265.
 - [30] H.A. Posch, W.G. Hoover, F.J. Vesely, Canonical dynamics of the Nose oscillator: stability, order, and chaos, *Phys. Rev. A* 33 (1986) 4253–4265.
 - [31] S. Meng, E. Kaxiras, Electron and hole dynamics in dye-sensitized solar cells: influencing factors and systematic trends, *Nano Lett.* 10 (2010) 1238–1247.
 - [32] W.-H. Liu, J.-W. Luo, S.-S. Li, L.-W. Wang, Impurity diffusion induced dynamic electron donors in semiconductors, *Phys. Rev. B* 100 (2019) 165203–165209.
 - [33] J.F. Li, Y.F. Huang, Y. Ding, Z.L. Yang, S.B. Li, X.S. Zhou, F.R. Fan, W. Zhang, Z. Y. Zhou, D.Y. Wu, B. Ren, Z.L. Wang, Z.Q. Tian, Shell-isolated nanoparticle-enhanced Raman spectroscopy, *Nature* 464 (2010) 392–395.
 - [34] Z.D. Schultz, S.K. Shaw, A.A. Gewirth, Potential dependent organization of water at the electrified metal-liquid interface, *J. Am. Chem. Soc.* 127 (2005) 15916–15922.
 - [35] W.T. Liu, Y.R. Shen, In situ sum-frequency vibrational spectroscopy of electrochemical interfaces with surface plasmon resonance, *P. Natl. Acad. Sci. USA* 111 (2014) 1293–1297.
 - [36] W.-H. Liu, J.-W. Luo, S.-S. Li, L.-W. Wang, Microscopic force driving the photoinduced ultrafast phase transition: time-dependent density functional theory simulations of IrTe₂, *Phys. Rev. B* 102 (2020) 184308–184316.
 - [37] Z. Liu, T. Lu, Q. Chen, An sp-hybridized all-carboatomic ring, cyclo[18]carbon: electronic structure, electronic spectrum, and optical nonlinearity, *Carbon* 165 (2020) 461–467.
 - [38] L. Wang, H. Xu, N. Jiang, Z. Wang, J. Jiang, T. Zhang, Trace cupric species triggered decomposition of peroxymonosulfate and degradation of organic pollutants: Cu(III) being the primary and selective intermediate oxidant, *Environ. Sci. Technol.* 54 (2020) 4686–4694.
 - [39] C. Kim, J.Y. Ahn, T.Y. Kim, W.S. Shin, I. Hwang, Activation of persulfate by nanosized zero-valent iron (NZVI): mechanisms and transformation products of NZVI, *Environ. Sci. Technol.* 52 (2018) 3625–3633.
 - [40] H. Tang, Z. Dai, X. Xie, Z. Wen, R. Chen, Promotion of peroxydisulfate activation over Cu_{0.84}Bi_{2.08}O₄ for visible light induced photodegradation of ciprofloxacin in water matrix, *Chem. Eng. J.* 356 (2019) 472–482.
 - [41] L.S. Zhang, X.H. Jiang, Z.A. Zhong, L. Tian, Q. Sun, Y.T. Cui, X. Lu, J.P. Zou, S. L. Luo, Carbon nitride supported high-loading Fe single-atom catalyst for activation of peroxymonosulfate to generate ¹O₂ with 100% selectivity, *Angew. Chem. Int. Ed.* 60 (2021) 21751–21755.
 - [42] Y. Gao, T. Wu, C. Yang, C. Ma, Z. Zhao, Z. Wu, S. Cao, W. Geng, Y. Wang, Y. Yao, Y. Zhang, C. Cheng, Activity trends and mechanisms in peroxymonosulfate-assisted catalytic production of singlet oxygen over atomic metal-N-C catalysts, *Angew. Chem. Int. Ed.* 60 (2021) 22513–22521.
 - [43] X. Mi, P. Wang, S. Xu, L. Su, H. Zhong, H. Wang, Y. Li, S. Zhan, Almost 100% peroxymonosulfate conversion to singlet oxygen on single-atom CoN₂₊₂ sites, *Angew. Chem. Int. Ed.* 60 (2021) 4588–4593.
 - [44] H. Li, J. Li, Z. Ai, F. Jia, L. Zhang, Oxygen vacancy-mediated photocatalysis of BiOCl: reactivity, selectivity, and perspectives, *Angew. Chem. Int. Ed.* 57 (2018) 122–138.
 - [45] H. Li, J. Tian, F. Xiao, R. Huang, S. Gao, F. Cui, S. Wang, X. Duan, Structure-dependent catalysis of cuprous oxides in peroxymonosulfate activation via nonradical pathway with a high oxidation capacity, *J. Hazard Mater.* 385 (2020) 121518–121526.
 - [46] E.T. Yun, J.H. Lee, J. Kim, H.D. Park, J. Lee, Identifying the nonradical mechanism in the peroxymonosulfate activation process: singlet oxygenation versus mediated electron transfer, *Environ. Sci. Technol.* 52 (2018) 7032–7042.
 - [47] J. Lee, U. von Gunten, J.H. Kim, Persulfate-based advanced oxidation: critical assessment of opportunities and roadblocks, *Environ. Sci. Technol.* 54 (2020) 3064–3081.
 - [48] W. Ren, L. Xiong, X. Yuan, Z. Yu, H. Zhang, X. Duan, S. Wang, Activation of peroxydisulfate on carbon nanotubes: electron-transfer mechanism, *Environ. Sci. Technol.* 53 (2019) 14595–14603.
 - [49] C. Cheng, W. Ren, F. Miao, X. Chen, X. Chen, H. Zhang, Generation of Fe(IV)=O and its contribution to Fenton-like reactions on a single-atom iron-N-C catalyst, *Angew. Chem. Int. Ed.* 62 (2023), e202218510.
 - [50] G.R. Raymond, Y.N. Ho, Ben L. Feringa, Lawrence Que Jr., RRaman evidence for a weakened O-O bond in mononuclear low-spin iron(III)-hydroperoxides, *J. Am. Chem. Soc.* 121 (1999) 264–265.
 - [51] X. Duan, Z. Ao, H. Sun, L. Zhou, G. Wang, S. Wang, Insights into N-doping in single-walled carbon nanotubes for enhanced activation of superoxides: a mechanistic study, *Chem. Commun.* 51 (2015) 15249–15252.
 - [52] Y. Chen, G. Zhang, H. Liu, J. Qu, Confining free radicals in close vicinity to contaminants enables ultrafast Fenton-like processes in the interspacing of MoS₂ membranes, *Angew. Chem. Int. Ed. Engl.* 58 (2019) 8134–8138.
 - [53] Z. Wang, E. Almatrafi, H. Wang, H. Qin, W. Wang, L. Du, S. Chen, G. Zeng, P. Xu, Cobalt single atoms anchored on oxygen-doped tubular carbon nitride for efficient peroxymonosulfate activation: simultaneous coordination structure and morphology modulation, *Angew. Chem. Int. Ed.* 61 (2022), e202202338.
 - [54] C. Lian, M. Guan, S. Hu, J. Zhang, S. Meng, Photoexcitation in solids: first-principles quantum simulations by real-time TDDFT, *Adv. Theory Simul.* 1 (2018) 1800055–1800065.
 - [55] J. Kuntail, U. Kumar, I. Sinha, Insight into photo-Fenton reaction mechanism on a magnetite-GO nanocomposite: computational and experimental investigations, *Mol. Catal.* 528 (2022) 112491–112501.
 - [56] X.Y. Liu, Z.W. Li, W.H. Fang, G. Cui, Nonadiabatic exciton and charge separation dynamics at interfaces of zinc phthalocyanine and fullerene: orientation does matter, *J. Phys. Chem. A* 124 (2020) 7388–7398.
 - [57] H. Choi, D. Shin, B.C. Yeo, T. Song, S.S. Han, N. Park, S. Kim, Simultaneously controllable doping sites and the activity of a W-N codoped TiO₂ photocatalyst, *ACS Catal.* 6 (2016) 2745–2753.